Characterization of the physicochemical properties of novel SnS2 with cubic structure and diamond-like Sn sublattice

7 AUTHORS, INCLUDING:

Hailei Zhao
University of Science and Technology Beijing
169 PUBLICATIONS **2,011** CITATIONS

SEE PROFILE

Anita Trenczek-Zając
AGH University of Science and Technology i…
23 PUBLICATIONS **327** CITATIONS

SEE PROFILE

Konrad Świerczek
AGH University of Science and Technology i…
92 PUBLICATIONS **735** CITATIONS

SEE PROFILE

Characterization of the physicochemical properties of novel SnS₂ with cubic structure and diamond-like Sn sublattice

Xin Liu,[a,b] Hailei Zhao,[a,*] Andrzej Kulka,[b] Anita Trenczek-Zając,[c] Jingying Xie,[d] Ning Chen[a] and Konrad Świerczek[b]

[a]*School of Materials Science and Engineering, University of Science and Technology Beijing, Xueyuan Road 30, Haidian District, Beijing 100083, People's Republic of China*
[b]*AGH University of Science and Technology, Faculty of Energy and Fuels, Department of Hydrogen Energy, al. A. Mickiewicza 30, 30-059 Krakow, Poland*
[c]*AGH University of Science and Technology, Faculty of Materials Science and Ceramics, Department of Inorganic Chemistry, al. A. Mickiewicza 30, 30-059 Krakow, Poland*
[d]*Shanghai Institute of Space Power Sources, Dongchuan Road 2965, Minhang District, Shanghai 200245, People's Republic of China*

Abstract—In this paper, a novel polymorph of SnS₂ having a cubic *Fd-3m* structure was prepared by a mechanochemical route; its lattice structure and thermal, electronic, transport, electrochemical and photoelectrochemical properties were systematically characterized. Structural studies indicated that no phase transition occurred in the −250 to 300 °C temperature range, with transition to ordinary trigonal *P-3m*1 phase followed by a significant sulfur loss at higher temperatures. The refined Sn–S interatomic distance of 2.5884(7) Å in the new phase is slightly higher than the one found in other polymorphs, while calculation of the energy gap E_g resulted in similar values (1.9 eV) for *Fd-3m* and *P-3m*1 structures. The recorded electrical conductivity has a thermally activated character with lower activation energy $E_a = 0.52(1)$ eV in the 40–160 °C range and 0.87(2) eV at temperatures exceeding 160 °C. Assuming that in the higher temperature range the conductivity is mainly intrinsic, the calculated $E_g = 2E_a \approx 1.7$ eV matches well the calculated E_g. The synthesized SnS₂ exhibits interesting photoelectrochemical properties, as well as good electrochemical characteristics when used as the anode material in lithium cells. In situ structural studies, performed during first discharge of such cells, clarified the nature of reaction of lithium with SnS₂, which was found to be complex, proceeding through intercalation-like, two-phase-like and decomposition-like stages.
© 2014 Acta Materialia Inc. Published by Elsevier Ltd. All rights reserved.

Keywords: SnS₂; Crystallography; Thermal analysis; Electrical properties; Li-ion battery

1. Introduction

In the phase diagram of the Sn–S binary system, there are three stoichiometric compounds known, with different tin to sulfur ratios: SnS, Sn₂S₃ and SnS₂ [1–3]. Tin disulfide belongs to a family of layered metal dichalcogenides, the crystal structure of which can be analyzed by considering strong ionic-covalent bonding between Sn and S (triple S–Sn–S layers) and weak van-der-Waals forces between these triple layers [4–6]. From another point of view, these structures can be described as being constructed from SnS₆ octahedra, connected only by their edges, forming layers. While the crystal structure of ordinary SnS₂ belongs to the trigonal system, with CdI₂-type structure and *P-3m*1 (No. 164) space group [7–9], it is known that different layer stackings give rise to many possible polytypes [10,11]. It is also important to mention literature data describing the properties of non-stoichiometric SnS₂-like materials [12]. In recent years many efforts have been made to finding unusual (e.g. carbon-related) polymorphs of SnS₂, which are expected to possess novel physicochemical properties. Fullerene-, nanotube- and single-octahedra-layer-like (graphene-like) SnS₂ materials have already been prepared and studied [13–16]. However, a diamond-like SnS₂ polymorph with cubic structure has never previously been reported.

As an *n*-type semiconductor with a band gap of ∼2 eV [17–19], SnS₂ is a multifunctional material, which can be used in many applications—photovoltaics, photocatalysis, gas sensing, etc. [20–24]. With a large interlayer spacing along the *c*-axis, alkali metal cations can be easily inserted into the interlayer space, and initially SnS₂ was considered as a candidate cathode material for primary lithium cells, delivering ∼585 mAh g⁻¹ specific capacity and a specific

energy density of $\sim$885 W h kg^{-1} with a cut-off voltage set as 1.1 V [25–27]. With the growth in interest in rechargeable batteries, research into SnS$_2$-based cathodes ceased, as the electrode process is not reversible in the considered potential range. Interestingly, if the cut-off voltage is lowered to, for instance 0.01 V, it is possible to insert much more lithium into the material, with total specific capacity exceeding 1200 mAh g^{-1}; however, the electrode process is in fact related to lithiation of tin embedded in the Li$_2$S matrix, due to lithiation and decomposition of Li$_x$SnS$_2$ [28]. In such composites, lithiation/delithiation is accompanied by relatively small volume changes of the anode, and is highly reversible, making the material attractive for rechargeable lithium-ion [29–33] and sodium-ion batteries [34,35].

Moreover, analyzing literature data on the microstructural properties of SnS$_2$, it can be observed that the morphology of the particle microstructure can be made plate-, rod-, belt-, flower-, hollow-like, as well as other forms, by the appropriate choice of preparation method and adjustment of the synthesis parameters [36–40]. This can be related to the layered-type structure, which makes such microstructural modifications relatively easy. It is obvious that from a point of view of possible applications, materials with such tailored microstructures are of particular interest.

This paper describes the characterization of SnS$_2$ with the *Fd-3m* cubic structure and diamond-like Sn connectivity; the material was prepared by a simple mechanical alloying method. We clarify the incorrectly identified berndite structure of mechanochemically prepared SnS$_2$, reported in previous works of other authors [41–44]. In addition to a detailed description of its structural features, the results of systematic studies of the thermal, electronic, transport, electrochemical and photoelectrochemical properties of the new SnS$_2$ polymorph are given.

2. Experimental

SnS$_2$ material was synthesized through a simple mechanochemical route with a planetary ball milling machine (PM100, Retsch). Tin and sulfur (both $\geqslant$ 99.5%, Sinopharm Chemical Reagent Co. Ltd.) powders were used as raw materials without any further purification. Respective powders were mixed in a stoichiometric ratio and placed in a stainless steel vial with stainless steel milling balls; the weight ratio of balls to powder was 20:1. Milling was performed in an argon atmosphere to prevent oxidation. The milling was conducted for 8 h with a rotation speed of 500 rpm. The purity of the sample was checked after the synthesis, and the iron content was found to be below detection level of energy-dispersive X-ray (EDX) spectroscopy, while X-ray photoelectron spectroscopy (XPS) studies estimated that the iron content did not to exceed 0.1 wt.%.

The crystal structure of the synthesized material was examined by X-ray diffraction (XRD) in the 10–110° range using Cu K_α radiation on a Panalytical Empyrean diffractometer equipped with a PIXcel3D detector. High-temperature XRD measurements (up to 300 °C, due to chemical stability concerns) were carried out in argon with an Anton Paar HTK 1200N oven-chamber installed. For low-temperature studies (down to −250 °C), an Oxford Instruments

cryostat was mounted, and the experiments were conducted under vacuum. Structural parameters were determined by the Rietveld method with the GSAS/EXPGUI set of software [45,46]. The minimal offset of data gathered using the room-, high- and low-temperature holders was small enough to be neglected. As the synthesized SnS$_2$ exhibits a cubic structure, the thermal expansion parameter was calculated as 1/3 of the relative unit cell volume expansion with temperature.

The morphology of the cubic SnS$_2$ material was studied by scanning electron microscopy (SEM) on a Hitachi S-4800 microscope equipped with an EDX analyzer. Additional measurements for the samples after heat treatment were conducted on FEI Nova NanoSEM 200 microscope.

XPS spectra were recorded on a RBD upgraded PHI-5000C ESCA system (Perkin Elmer) with Mg K_α radiation (hv = 1253.6 eV) under 5×10^{-8} Pa vacuum. The binding energies were referenced to the C$_{1s}$ peak (284.6 eV) from the surface adventitious carbon.

Thermogravimetric (TG) studies were conducted on TA Q5000IR thermobalance under 100 cm^3 min^{-1} of Ar (5N) flow with a 10 °C min^{-1} heating/cooling rate, using a 10 min equilibration time at the highest temperature of 300 °C. For the measurements, $\sim$20 mg of the powdered material was evenly placed on a Pt holder. For technical reasons (due to the evaporation of sulfur), it was not possible to reach higher temperatures. The buoyancy effect, which was established on a basis of runs performed with an empty holder, was found to be very small, and did not affect the measurements.

Optical reflectance spectra were recorded with a Lambda 19 Perkin-Elmer double-beam spectrophotometer equipped with a 150 mm integrating sphere over a wide wavelength range from 250 to 2500 nm.

The electrical conductivity σ was measured in Ar atmosphere in the 25–300 °C temperature range using the impedance method (Solartron 1260 Frequency Response Analyzer). A pressed disk 10 mm in diameter and 1.4 mm thick was painted on both sides with silver paste and placed in a custom-made holder. As it was not possible to sinter the pellet, due to low thermal stability of the cubic phase of SnS$_2$ (see below), in order to calculate the absolute values of the electrical conductivity, Bruggeman's effective medium approximation was used: with an estimated porosity of 40%, an appropriate porosity-related correction was taken into account [47]. The estimated relative error of σ was 10%, taking into account the accuracy of the measurements of sample's porosity and dimensions, as well as the analyzer used.

First-principles calculations were performed using Castep code embedded in Materials Studio (MS) software [48]. The band gap E$_g$ and density of states (DOS) of both cubic and hexagonal SnS$_2$ were calculated by the generalized-gradient-approximation with the revised Perdew–Burke–Ernzerhof exchange–correlation functional and the norm-conserved pseudopotential plane-wave method. Geometry optimization of the unit cell was performed by the BFGS algorithm; however, only atomic positions were refined as the lattice parameters from XRD refinements were considered correct and accurate. All the detailed parameters of the calculations were set up the same as in Ref. [49].

Current–voltage (I–V) characteristics were recorded in a photoelectrochemical cell (PEC). For this purpose, the powder was pressed into pellets with diameter of 0.8 cm

in diameter, which were then used as photoanodes. Platinum foil covered with platinum black served as the cathode, and a saturated calomel electrode (SCE) as a reference electrode. All electrodes were immersed in a 0.8 M Na_2SO_4 solution (for further details see Ref. [50]).

In situ XRD measurements were performed in the 25–60° range using Cu K_α radiation on a Panalytical Empyrean diffractometer. A custom-made gas-tight cell for these studies was made from Teflon and stainless steel containers, joined by screws and sealed by gaskets. A beryllium window, placed on the SnS_2 side, acted as both an X-ray-transparent medium and a current collector. SnS_2 layers, suitable for in situ XRD measurements, were prepared on aluminum foil, as X-ray transmission through (light) aluminum is much easier than in the case of copper foil. To prevent lithiation of aluminum (occurring at $\sim$0.3 V vs. metallic lithium), the low-voltage cut-off was set at 0.5 V and the measurements were performed only during the first discharge of the $Li/Li^+/Li_xSnS_2$ cell. In order to keep the notation of the lithium cells simple, the working material is written as Li_xSnS_2, despite complex lithiation process, as described in this paper. For preparation of the layers, SnS_2 (80 wt.%) powder mixed with carbon black (10 wt.%) was used as a conductive agent, and polyvinylidene difluoride (10 wt.%) was used as a binder. 1 M $LiPF_6$ dissolved in 50:50 vol.% ethylene carbonate (EC)/diethylene carbonate (DEC) served as the electrolyte. In order to calibrate position of the layer in relation to the diffractometer's geometry, initial in situ patterns were compared with ex situ XRD data for the identical SnS_2-based layer. The electrochemical tests during in situ XRD measurements were performed using an Autolab PGSTAT302N potentiostat/galvanostat. The first discharge was recorded with C/70 constant current density.

In order to achieve better performance during cycling, for other electrochemical tests, SnS_2-based layers and cells were prepared in a different way. SnS_2-based electrodes were made with carboxymethyl cellulose (CMC) and vapor-grown carbon fibers (VGCF) as binder and conductivity agent, respectively. SnS_2 powder (80 wt.%), VGCF (10 wt.%) and CMC (10 wt.%) were mixed for 12 h in deionized water. The obtained slurry was put onto the copper foil with a surgical scalpel. The prepared layer was dried at room temperature for 2 h and then at 120 °C for 6 h under vacuum. The diameter of the electrode plates was 14 mm. The cells were assembled in an argon-filled glovebox with moisture and oxygen content kept below 1 ppm. Celgard 2325 film was used as a separator, while 1 M $LiPF_6$ dissolved in EC/ethyl methyl carbonate (EMC)/dimethyl carbonate (DMC)/fluoroethylene carbonate (FEC) (30:30:30:10 by volume) was used as the electrolyte. The cells were tested using battery testers (LANDCT2001A, Land). For the tests, the voltage cut-off was set at 0.01 and 1.5 V. A current density of 0.1 A g^{-1} was used for cycling performance tests; however, different values ranging from 0.1 up to 2.0 A g^{-1} were applied for rate capability measurements.

3. Results and discussion

3.1. Crystal structure and microstructure

To date, the structural properties of mechanochemically synthesized SnS_2 have been reported in at least four papers

[41–44]. Identification of the structure of the considered material was done by comparison with JCPDS-ICDD 00-023-0677 pattern (PDF4 + 2012); however, there is no peak present at $\sim$38° in the reference, while this peak is clearly seen in the measured pattern. There are also several other incorrectly assigned peaks, which allow us to conclude that the previous identification was incorrect. In more recent reports by Balaz et al. [42,43], the structural data of mechanochemically synthesized SnS_2 with initial Sn:S proportion equal to 1:1.85 was identified as a mixture of two phases: one being berndtite SnS_2 ($4H$, $P6_3mc$) and one new $4H$-like, but given without further description. As the referenced JCPDS-ICDD 00-021-1231 pattern shows significantly different intensities of majority of the peaks of the $P6_3mc$ phase, this report too is likely incorrect. Moreover, the XRD data reported in all of the mentioned papers are qualitatively the same.

However, the recorded XRD data for the studied SnS_2 (Fig. 1a) could be successfully refined assuming a single-phase, cubic structure with Fd-$3m$ symmetry. Information about the main peaks of this structure is presented in Table 1. In addition, the refined structural parameters are included in Table 2, while visualization of this cubic structure is shown in Fig. 1b. As can be seen, contrary to the majority of SnS_2 polymorphs, which exhibit a layered-type arrangement of SnS_6 octahedra (2-D structure) [7–11], in the novel, cubic structure of SnS_2, the arrangement of the octahedra can be considered as forming a 3-D network. In addition, it is worth mentioning that the structure is not a closely packed one, as the $16d$ (1/2, 1/2, 1/2) position is empty. The possible presence of Sn at the $16d$ position was considered in the performed Rietveld refinements, but was found not to exceed 1%.

The formation of such a crystal structure, likely metastable, may be linked to the mechanochemical method used for the preparation of the material [51]. In a synthesis procedure of this type, the formation of a layered-type structure is not favored, while at the same time, a structure consisting of a 3-D arrangement of SnS_6 octahedra should form more easily. Nevertheless, in both structures the octahedra share edges only, with each oxygen belonging to three neighboring octahedra. Furthermore, the average Sn–S distance is similar in both structures (Table 2), and additionally the Sn–S–Sn angle is close to 90°. The calculated theoretical density is somewhat lower for the cubic phase, corresponding well with a bigger Sn–S distance.

One additional comment about the reported crystal structure can be made: the connectivity of SnS_6 octahedra resembles that of C atoms in the diamond structure [52]. Alternatively, it is also possible to say that the connectivity of Sn atoms (with a Sn–Sn distance equal to $\sim$3.65 Å) is similar to that in diamond (though the C–C distance is much smaller). Interestingly, in layers formed by SnS_6 octahedra in ordinary SnS_2 polytypes, the connectivity of S atoms in the respective S-related layers is similar to that of C atoms in graphite. Nevertheless, the similar Sn–S distance and the shape of the octahedra in both the cubic and hexagonal structures of SnS_2 allow us to assume that many physicochemical properties of the polymorphs should not differ considerably (see below).

In addition to the room-temperature studies, XRD data were also measured in the −250 to 300 °C temperature range (Fig. 2). No structural transformation was observed in this range, with unit cell volume changes with temperature being close to linear at T > −50 °C. This dependence

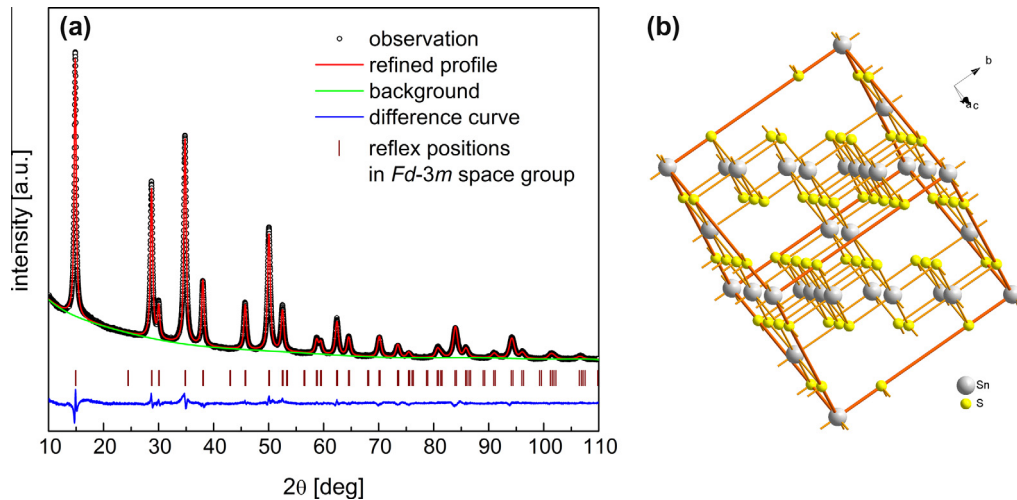**Fig. 1.** (a) XRD diffractogram with Rietveld refinement. (b) Visualization of the cubic *Fd-3m* structure of the considered SnS₂.

Table 1. Selected peaks (with relative intensities >10%) for the refined cubic structure of SnS₂.

2θ [deg]	h	k	l	d-spacing [Å]	I(111) [%]
14.863	1	1	1	5.9555	100.00
28.679	1	1	3	3.1102	60.70
29.984	2	2	2	2.9778	14.43
34.759	0	0	4	2.5788	88.22
37.992	1	3	3	2.3665	27.69
45.663	1	1	5	1.9852	14.55
49.976	0	4	4	1.8235	53.69
52.436	1	3	5	1.7436	18.62
62.312	4	4	4	1.4889	16.21
83.813	0	4	8	1.1533	17.31

Table 2. Refined structural parameters of the cubic SnS₂.

Property	Value
Space group	*Fd-3m*
Unit cell parameter a [Å]	10.3152(2)
Unit cell volume V [Å³]	1097.58(5)
Sn(1) 16c	(0, 0, 0)
S(1) 32e	(x, x, x) $x = 0.2509(1)$
Density (*Fd-3m*) ρ [g cm⁻³]	4.425
Density (*P-3m1*)[a] ρ [g cm⁻³]	4.46–4.50
Sn–S distance (*Fd-3m*) [Å]	2.5884(7)
Sn–S distance (*P-3m1*)[a] [Å]	2.56–2.57
Grain size calculated from Scherrer's formula [nm]	21
Average primary particle size (from SEM) [nm]	36
Average secondary particle size (from SEM) [µm]	1.5

[a] Calculated using structural data from Refs. [7,49].

allowed the linear thermal expansion coefficient (TEC) to be calculated, and an estimate of $9.4(3) \times 10^{-6}\,\mathrm{K^{-1}}$ was obtained for the temperature range −50 to 300 °C. This value is typical for many sulfides and oxides [53].

Fig. 3a and b show SEM micrographs of the obtained powder taken at different magnifications. Statistical analysis of the pictures allowed us to calculate the average secondary particle size (of aggregates and agglomerates) as 1.5 µm, with the majority being <5 µm. In addition, the primary particle size was estimated as being in the range 10–90 nm, with an average of 36 nm. For comparison, the crystallite size calculated using Scherrer's formula was found to be 21 nm, matching well the average primary particle size (Table 2). Such a structure is typical for a product of mechanochemical synthesis [54]. During microstructural studies additional EDX measurements were performed (Fig. 3c), which confirmed the sample homogeneity and the assumed Sn:S ratio in the considered material.

Fig. 4a shows a survey XPS spectrum of the cubic SnS₂. The main peaks can be related to Sn, S, as well as C and O elements. C and O signals come from some contamination present on the surface of the sample, as often observed in XPS tests [55]. The measured atomic ratio of Sn and S is 1:1.73. However, the surface-only detection ability of the XPS method has to be taken into account. The content of other elements was also checked in the spectrum, but was found to be below the detection accuracy of the XPS apparatus (<0.2 at.%). The core-level spectra of Sn 3d and S 2p are shown in Fig. 4b and c. Peaks at 161.7, 486.5 and 490.0 eV can be assigned to S 2p, Sn 3$d_{5/2}$ and Sn 3$d_{3/2}$, respectively, which agrees well with the reported data for SnS₂ [56]. Also, this agrees well with structural refinement, showing the single-crystallographic position for Sn and S (Table 2). No peaks corresponding to Sn²⁺ (at 485.8 eV [57]) or elemental Sn (at 485.0 eV [58]), as well as elemental S (at 164.05 eV [59]) were detected. Thus the

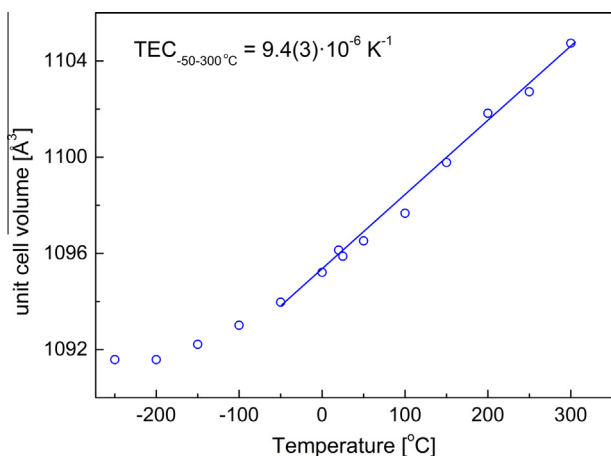**Fig. 2.** Unit cell dependence on temperature with calculated TEC for the SnS_2 compound investigated in this paper.

XPS measurements further confirm the chemical composition of the prepared SnS_2.

3.2. Thermal stability of cubic SnS_2

Due to the mechanochemical synthesis method used here, cubic SnS_2 is expected to be thermodynamically metastable, and will likely transform to normal, hexagonal structure at high temperatures. In addition, significant absorption of gases (H_2O, CO_2) can be anticipated with such SnS_2 powder, as the material's primary particles are nanometer sized. TG experiments (Fig. 5), performed in argon (5N) atmosphere up to 300 °C, revealed a large mass decrease on the first cycle, which may be connected to a desorption of gases from the surface of the grains; however, on subsequent cycles only a small mass loss was recorded, and only above 270 °C. Supporting XRD studies (Fig. 6a), performed after annealing of the material at 300 °C for 2 h in argon, indicated stability of the cubic SnS_2 up to this temperature, but with the intensity of the (1 1 1) peak decreasing, likely related to the sulfur loss mentioned above. After annealing at 400 °C the material consisted of a mixture of cubic and hexagonal phase (note the double peak shown in Fig. 6a inset), while after annealing at 500 °C the dominant phase was Sn_2S_3, indicating significant loss of sulfur. Such results confirm the metastability of the cubic SnS_2, which transforms to stable hexagonal phase upon heating. The thermal stability of the hexagonal SnS_2 was also reported in 10^{-6} torr vacuum up to 550 °C [60]. Comparing both these results, one has to remember that nanosized materials are more reactive. Additional annealing performed at 750 °C for the cubic SnS_2 resulted in formation of SnS with an interesting, layered microstructure, which can be seen in Fig. 6b.

3.3. Energy gap, transport properties and electronic structure calculations

The recorded optical reflectance spectra for the SnS_2 powder examined in this paper is given in Fig. 7a. One can see a significant change in the spectral dependence of reflectance: in the 400–650 nm range an abrupt increase in the reflectance was observed, indicating an onset of the fundamental absorption edge, as typically observed for
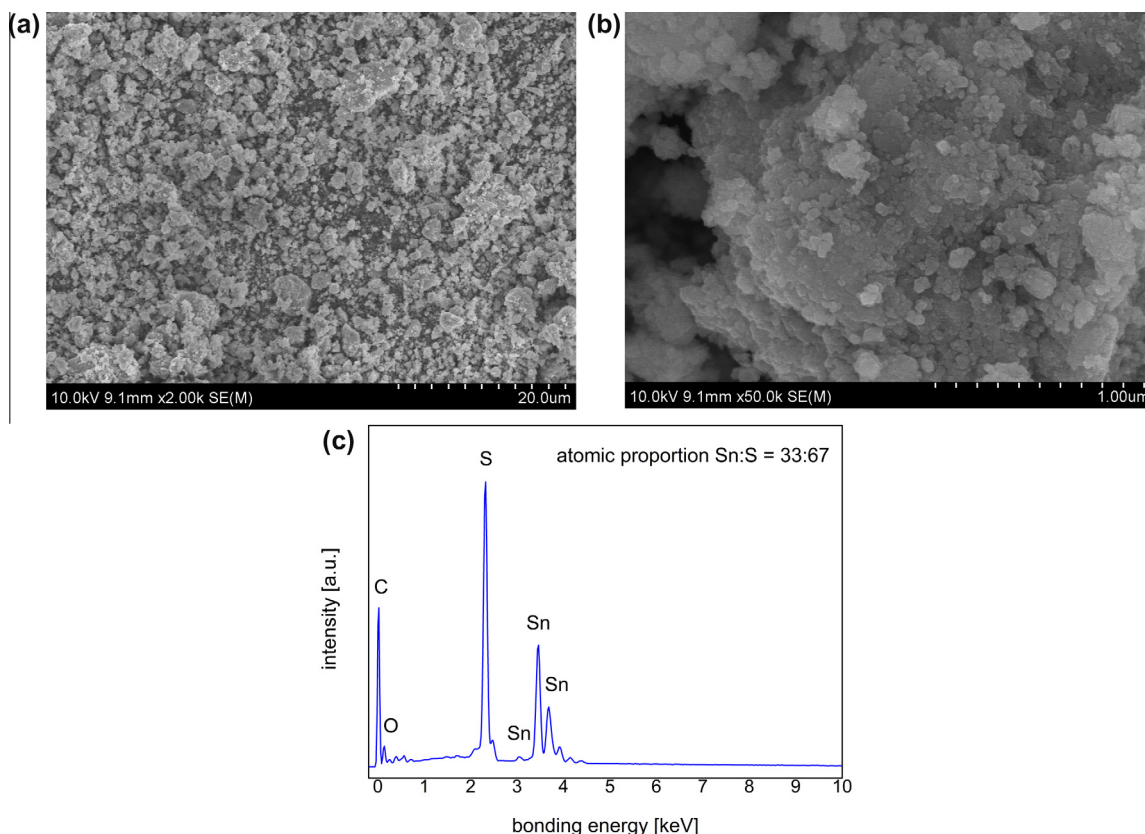

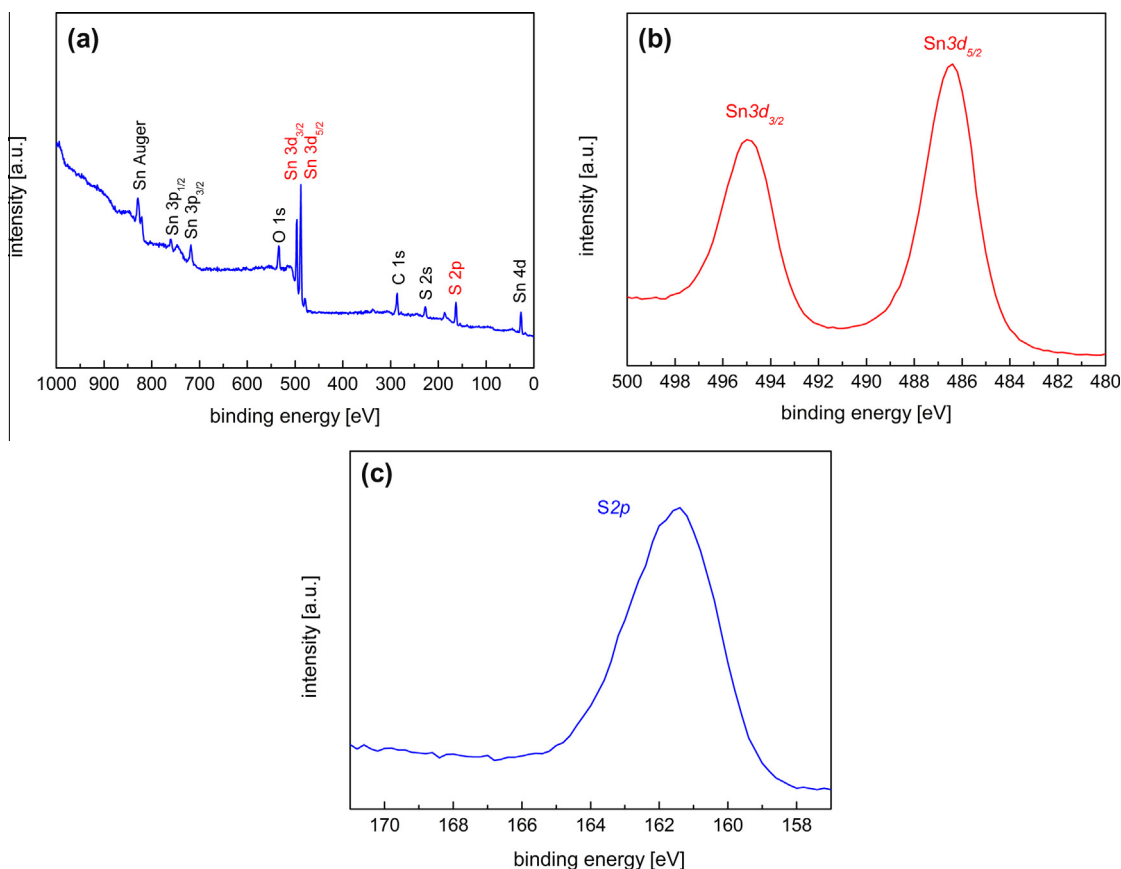**Fig. 3.** (a, b) SEM micrographs at different magnifications. (c) EDX data gathered for the SnS_2 powder.

Fig. 4. (a) Measured XPS spectrum for the considered SnS_2 and core-level spectrum for (b) Sn $3d$ and (c) S $2p$.
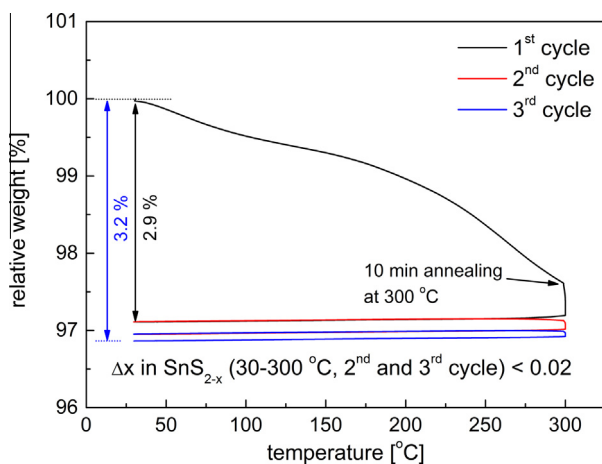

Fig. 5. Thermogravimetric studies of SnS_2 powder in Ar atmosphere for the first three cycles up to 300 °C.

semiconductors. The band-gap energy E_g was determined by an appropriate fitting of the Kubelka–Munk function (K–M), calculated directly from the diffused reflectance spectra (Fig. 7b) [61]. A transition energy equal to 2.3(1) eV was found, but it is known that such experiments may overestimate the actual value, and in the case of indirect gap-type semiconductors, the recorded value cannot be associated directly with the energy gap E_g, as typically only direct transitions are observed with electron–photon interactions [62].

SnS_2 is considered as intrinsic *n*-type semiconductor [1]. Interestingly, the reported values of the electrical conductivity vary strongly from $\sim 10^{-7}$ to 0.9 S cm^{-1} [17,19,63]. The results of the electrical conductivity measurements are given in Fig. 8a and b. As can be seen in Fig. 8b, the extrapolated value of σ at 25 °C is $\sim 5 \times 10^{-9}$ S cm^{-1}. The calculated activation energy E_a of σ changes to 0.52(1) eV at lower temperatures, but increases to 0.87(2) eV at temperatures exceeding 160 °C. Assuming that at higher temperatures the electrical conductivity is mainly intrinsic with ($E_g = 2E_a$), the E_g can be estimated from the higher temperature range as 1.7 eV, which is comparable to calculated value (1.9 eV, see below) and the optical results shown above. The lower E_a at lower temperatures can be associated with the presence of crystal defects, which originate from the mechanochemical synthesis; however, no measurable amount of Sn^{2+} was found from XPS studies. The recorded impedance spectra did not allow the bulk and the grain boundary contributions to the total conductivity to be distinguished. Finally, one has to remember that due to the instability of the cubic SnS_2 at higher temperatures it was not possible to prepare dense pellets of the material, so the electrical conductivity results, especially in terms of the absolute values, may contain some errors.

The band structure, total and partial densities of states of the cubic SnS_2 are shown in Fig. 9. The material is an indirect band gap-type semiconductor with a calculated band gap of ~ 1.9 eV. As expected, the value is slightly lower than the one obtained from the optical experiments. For comparison, E_g of the hexagonal SnS_2 was also calculated with the same set of parameters, and the value was
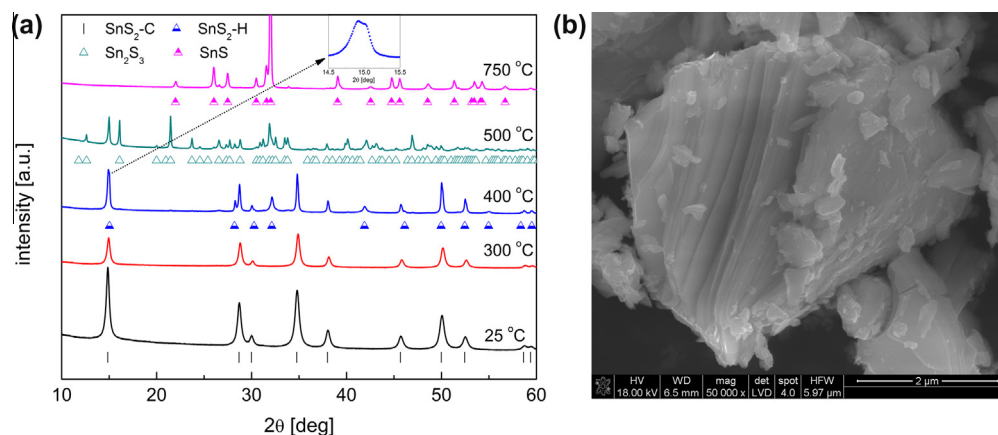
Fig. 6. (a) XRD diffractograms recorded for SnS$_2$ annealed at different temperatures. (b) SEM micrographs of the material annealed at 750 °C (with SnS composition).
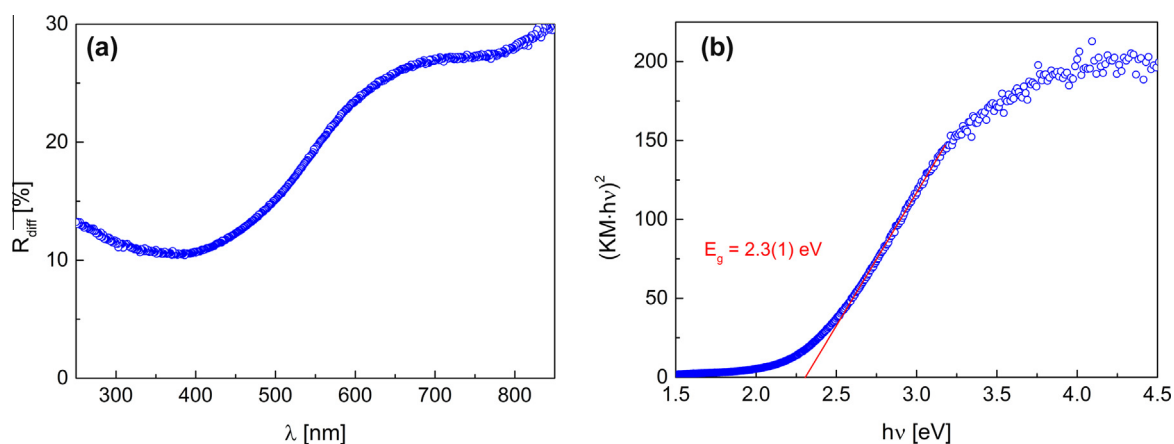

Fig. 7. (a) Diffused reflectance spectra for SnS$_2$ powder. (b) Determination of the band-gap energy E$_g$, calculated appropriately using the Kubelka–Munk function.
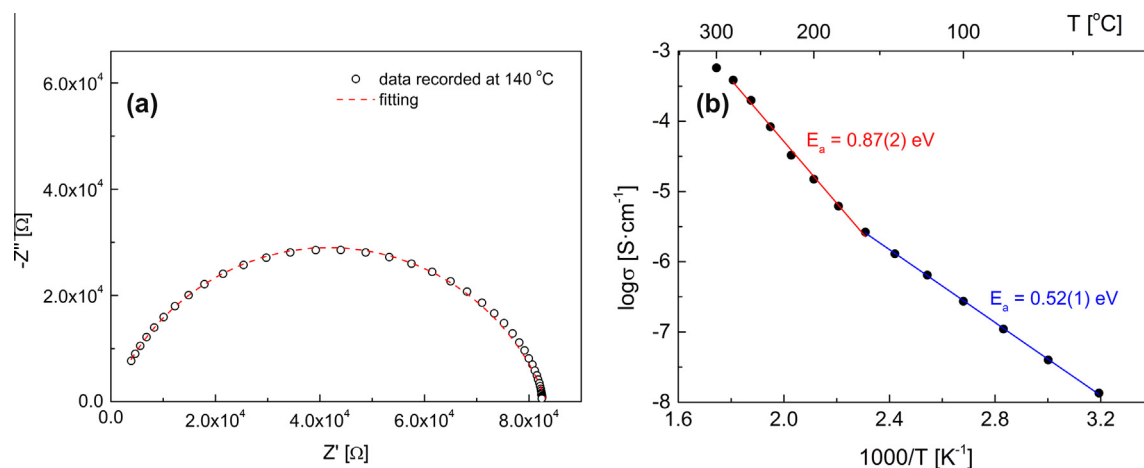

Fig. 8. (a) Typical recorded impedance spectra. (b) Temperature dependence of the electrical conductivity of the SnS$_2$ pellet.

found to be almost identical to the cubic one. However, the band gap of hexagonal SnS$_2$ from Ref. [49], calculated using the same software and initial parameters, but without unit cell parameter optimization, was reported as 2.1 eV. The reported DOS of the considered SnS$_2$ originates from the Sn$_{s,p}$ and S$_{s,p}$ electron contributions, similar to the hexagonal form [64]. The valence band at −5 to 0 eV is mostly due to p electrons.
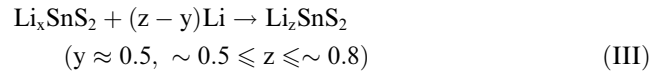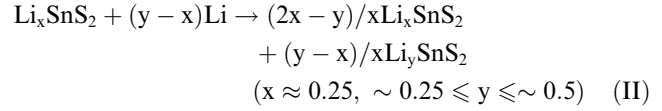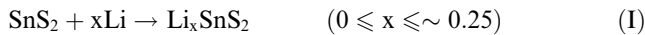
3.4. Photoelectrochemical properties of cubic SnS$_2$

As an example of the photoelectrochemical behavior of the SnS$_2$ electrode, the current–voltage (I–V) relationship is presented in Fig. 10. The current density ΔI_{ph} is expressed as the difference between the current recorded upon illumination with a white light and the current obtained without illumination. The flat-band potential of photoanode V$_{fb}$ is

an important parameter: it should be negative in order to separate the electrons from its holes and restrict the recombination process [65]. The value of V_{fb} was obtained from the recorded ΔI_{ph}–V curve, and was assumed to be equal to the potential value at the onset of the anodic photocurrent. In the case of the studied SnS_2 photoanode, the V_{fb} is negative and equals $-140(5)$ mV.

3.5. Electrochemical properties of cubic SnS$_2$

In order to understand electrochemical lithiation of cubic SnS_2 better, the first discharge process was analyzed by in situ XRD; to our knowledge this is the first time this has been done for SnS_2 (Fig. 11). The observed change in the XRD patterns is complex, but can be divided into the following six parts. During the initial lithiation (cell voltage down to ~2.0 V) SnS_2-related peaks shift towards lower angles, indicating that the unit cell becomes bigger, and suggesting an intercalation-like process (incorporation of lithium into the crystal structure occurring without major changes to the structure, Li_xSnS_2). As more lithium is introduced, the peaks do not shift, but new peaks appear, with increasing intensity. The new phase (Li_ySnS_2) can be refined with the cubic $Fd\bar{3}m$ cell as well, with the a parameter of the order of 10.8 Å, which represents an ~5% increase compared to the pristine material. Therefore, the first plateau at ~1.9 V can be related to the two-phase-like mechanism of lithiation. However, the following plateau (at ~1.8 V) corresponds to a presence of single phase only (Li_zSnS_2, z > y), with peaks again shifting towards lower angles. The voltage drop down to ~1.2 V, occurring in the next section, can be related to a complex process of further lithiation of Li_zSnS_2, but also to a partial decomposition of the material, with the following part related to the lithiation of sulfur up to Li_2S composition (with voltage in the range of ~0.8–1.1 V) [28,36]. It is known that lithiation of tin occurs at a lower voltage range (<0.7 V) [66]. This step is also visible in the in situ studies performed, though with a very broad and not intense peak appearing near 27° [67]. Based on our analysis of the in situ XRD results, the initial lithiation process of the cubic SnS_2 can be expressed as occurring according to the equations presented below (essentially, this process is qualitatively similar to the one observed for the hexagonal polymorph [25–28,36]):

$$SnS_2 + xLi \rightarrow Li_xSnS_2 \qquad (0 \leqslant x \leqslant \sim 0.25) \qquad (I)$$

$$\begin{aligned} Li_xSnS_2 + (y - x)Li &\rightarrow (2x - y)/xLi_xSnS_2 \\ &+ (y - x)/xLi_ySnS_2 \\ &(x \approx 0.25, ~\sim 0.25 \leqslant y \leqslant \sim 0.5) \quad (II) \end{aligned}$$

$$\begin{aligned} Li_xSnS_2 + (z - y)Li &\rightarrow Li_zSnS_2 \\ &(y \approx 0.5, ~\sim 0.5 \leqslant z \leqslant \sim 0.8) \qquad (III) \end{aligned}$$

further lithiation of Li_zSnS_2 and its decomposition into

Sn and lithium sulfide   (IV)

further lithiation with formation of Li_2S matrix

and inactive (in this voltage range) Sn   (V)

$$Sn + 2Li_2S_{(inactive)} + aLi \rightarrow Li_aSn + 2Li_2S_{(inactive)} \qquad (VI)$$

It is likely that the Li_2S-like matrix that forms (the inactive component of the anode) is amorphous, and therefore not visible in the studies reported here. Also, it was not possible to observe peaks related to metallic tin. Unfortunately, due to technical reasons, data in the lower angular range could not be used.

The electrochemical performance of cubic SnS_2 material anode was measured in $Li/Li^+/Li_xSnS_2$ cells. Fig. 12a shows discharge/charge curves measured during the first
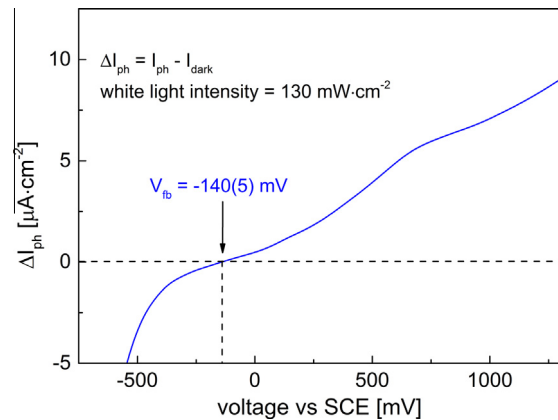

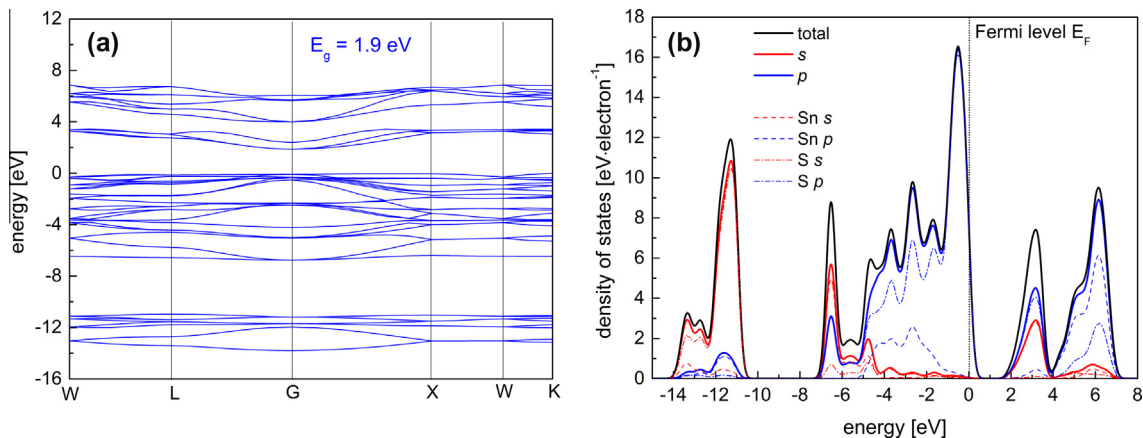**Fig. 10.** Current–voltage characteristics for the SnS_2 photoelectrode in PEC.

Fig. 9. Calculated (a) electronic structure and (b) density of states for the cubic SnS_2.
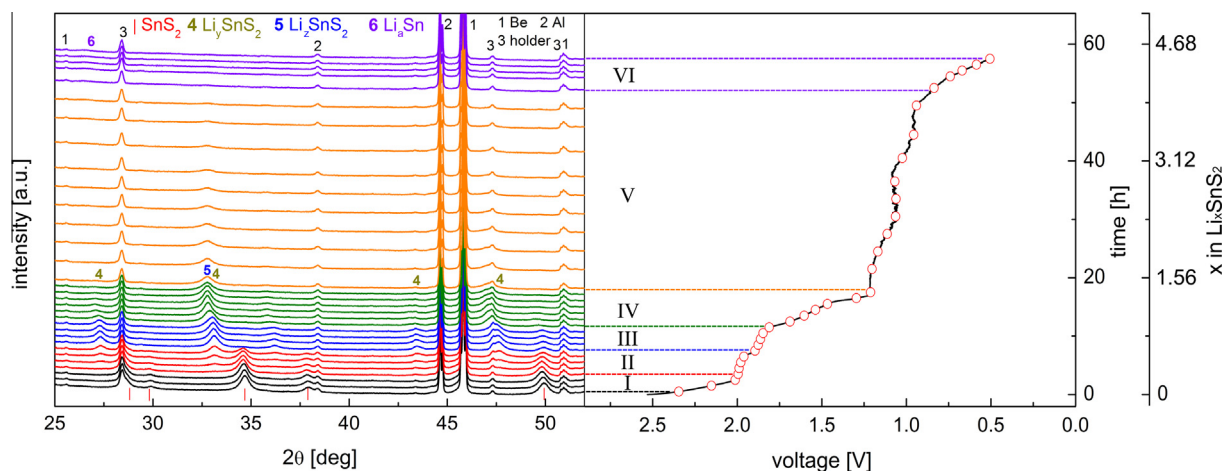
Fig. 11. In situ XRD studies during the first discharge of the Li/Li$^+$/Li$_x$SnS$_2$ cell.

three cycles. The initial discharge capacity of the material is equal to ~1400 mAh g^{-1}, while during charging the recorded capacity exceeded 655 mAh g^{-1}, corresponding to an initial coulombic efficiency of 46.8%. As explained above, during the initial discharge SnS$_2$ lithiates, and then decomposes in the presence of inactive Li$_2$S. Assuming that only Sn is electrochemically active, and that the highest lithium content is the Li$_{4.4}$Sn compound [68], the observed charge capacity can be directly related to full delithiation of Li$_{4.4}$Sn. During the second and third cycles the coulombic efficiency is ~97%. From the differential capacity curves

shown in the Fig. 12b, one can see four peaks at about 1.9, 1.8, 1.6 and 1.2 V in the high-voltage range of the first discharge curve. These peaks are not observed in the following cycles, due to the SnS$_2$ lithiation mechanism described above. Similar behavior was also shown during lithiation of hexagonal SnS$_2$ with the peaks appearing at about 1.9, 1.6 and 1.1 V [25–27]. In the low-voltage range (Fig. 12b), there is one irreversible peak and two pairs of reversible redox peaks at voltages of, respectively, 0.32, 0.24/0.43 and 0.08/0.14 V. The irreversible peak can be related to a formation of solid electrolyte interface (SEI)
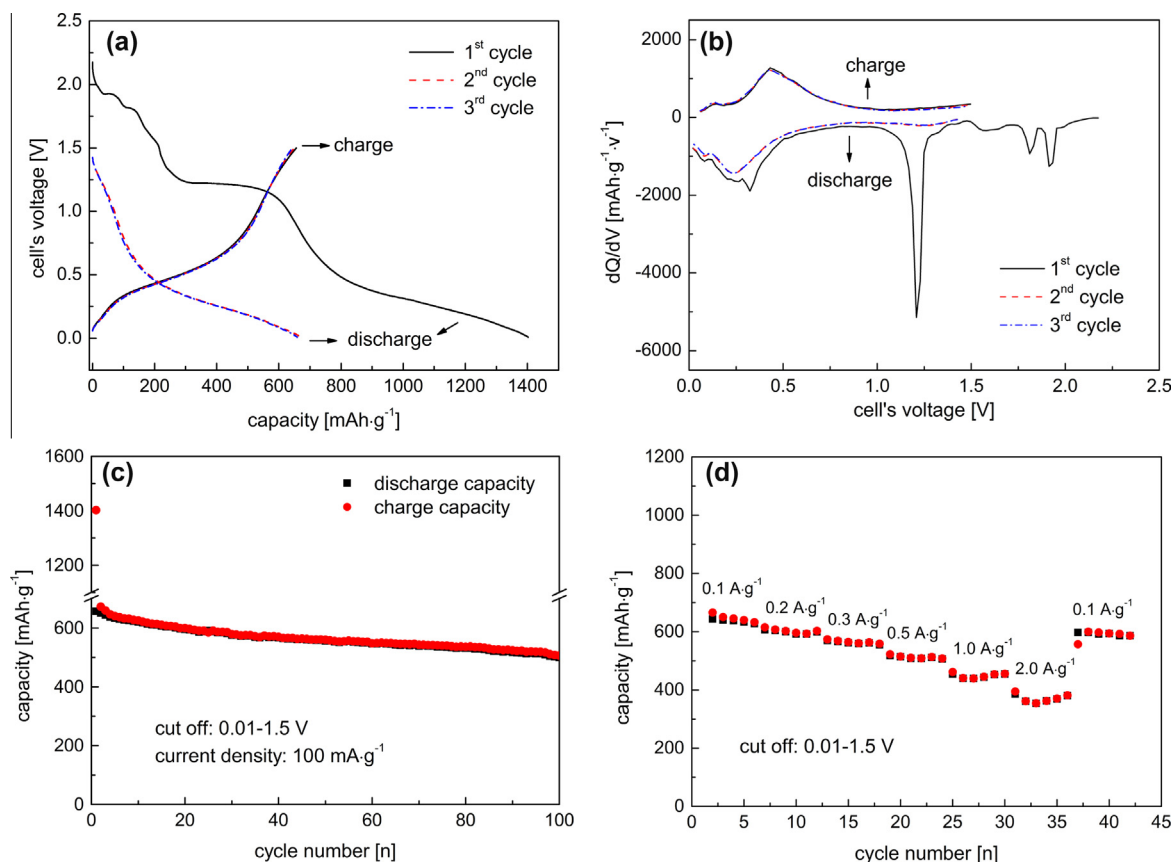

Fig. 12. (a) First three discharge/charge characteristics with (b) calculated differential capacity, (c) cycling performance and (d) rate capability (without the first cycle data) of the Li/Li$^+$/Li$_x$SnS$_2$ cell.

film, while the two pairs of redox peaks correspond to the multistep alloying reaction between Li and Sn [66,68].

The cycling performance of the studied cells is shown in Fig. 12c. Good properties, with a reversible capacity reaching almost 500 mAh g^{-1} retained after 100 discharge/charge cycles, was obtained. While the recorded reversible capacity is in the ordinary range expected for SnS$_2$-based anodes, the cycling performance is even better than in some results reported for the hexagonal SnS$_2$ with modified morphology [30–33,37–39]. As the density of cubic SnS$_2$ is lower than that of the hexagonal form (Table 1), during its reaction with lithium and decomposition it is expected to form less dense Li$_a$Sn/Li$_2$S anode composite, which should be able to accommodate the volume expansion during the lithiation process. In addition, inactive Li$_2$S phase buffers the volume change occurring during lithiation/delithiation of Sn. This in turn allows good stability of the electrode's microstructure, and hence is beneficial for the cycle performance. It is worth emphasizing that the measured capacity is much higher than that of commercial, carbon-based anode material ($\sim$330 mAh g^{-1} [69]).

The recorded rate capability the constructed cells is also good (Fig. 12d). At a current density in the 0.1–1.0 A g^{-1} range, the delivered capacity is 650–450 mAh g^{-1}. Even at a high current density of 2.0 A g^{-1}, the capacity is still 370 mAh g^{-1} with a retention ratio of 57% (in comparison to 0.1 A g^{-1} current density). When the current density was decreased back to 0.1 A g^{-1}, the capacity recovered to 600 mAh g^{-1}.

4. Conclusions

This paper reports the systematic characterization of the structural, thermal, electronic, transport, electrochemical and photoelectrochemical properties of a novel polymorph of SnS$_2$ with cubic *Fd-3m* structure. The material is stable up to $\sim$300 °C in argon, above which it transforms to hexagonal SnS$_2$, which is followed by loss of sulfur. The electrical conductivity of this compound has a thermally activated character with an indirect-type energy gap. Optical analysis revealed a fundamental absorption edge, which allowed the band gap energy to be calculated as 2.3 eV, while ab initio calculations gave E$_g$ = 1.9 eV. Photocurrent measurements over the ultraviolet and visible range of the light spectrum allow us to conclude that cubic SnS$_2$ can be considered as a promising candidate material for photoanodes. In situ XRD studies, performed during first discharge of the Li/Li$^+$/Li$_x$SnS$_2$ cell, clarified the nature of the reaction of Li with SnS$_2$, which was found to be complex, proceeding through intercalation-like, two-phase-like and decomposition-like stages. Good electrochemical characteristics were obtained with lithium cells in which cubic SnS$_2$ was used as the electrode material.

Acknowledgments

References

[1] L. Burton, D. Colombara, R. Abellon, F. Grozema, L. Peter, T. Savenije, et al., Synthesis, characterization, and electronic structure of single-srystal SnS, Sn$_2$S$_3$, and SnS$_2$, Chem. Mater. 25 (2013) 4908.

[2] L.S. Price, I.P. Parkin, A.M.E. Hardy, R.J.H. Clark, Atmospheric pressure chemical vapor deposition of tin sulfides (SnS, Sn$_2$S$_3$, and SnS$_2$) on glass, Chem. Mater. 11 (1999) 1792.

[3] L.A. Burton, A. Walsh, Phase stability of the earth-abundant tin sulfides SnS, SnS$_2$, and Sn$_2$S$_3$, J. Phys. Chem. C 116 (2012) 24262.

[4] C. Mondal, M. Ganguly, J. Pal, A. Roy, J. Jana, T. Pal, Morphology controlled synthesis of SnS$_2$ nanomaterial for promoting photocatalytic reduction of aqueous Cr(VI) under visible light, Langmuir 30 (2014) 4157.

[5] A. Umar, M.S. Akhtar, G.N. Dar, M. Abaker, A. Al-Hajry, S. Baskoutas, Visible-light-driven photocatalytic and chemical sensing properties of SnS$_2$ nanoflakes, Talanta 114 (2013) 183.

[6] C.A. Formstone, E.T. FitzGerald, P.A. Cox, P.A. Cox, D. OHare, Photoelectron spectroscopy of the tin dichalcogenides SnS$_{2-x}$Se$_x$ intercalated with cobaltocene, Inorg. Chem. 29 (1990) 3860.

[7] R.M. Hazen, L.W. Finger, The crystal structures and compressibilities of layer minerals at high pressure; I, SnS$_2$, berndtite, Am. Mineral. 63 (1978) 289.

[8] H.S. Song, S.L. Li, L. Gao, Y. Xu, K. Ueno, J. Tang, et al., High-performance top-gated monolayer SnS$_2$ field effect transistors and their integrated logic circuits, Nanoscale 5 (2013) 9666.

[9] D. Vollath, D.V. Szabo, Nanoparticles from compounds with layered structures, Acta Mater. 48 (2000) 953.

[10] G.B. Dubrovski, A.I. Shelykh, Photoelectric properties of tin disulfide, Phys. Solid State 40 (1998) 1295.

[11] A.N. Utyuzh, Y.A. Timofeev, G.N. Stepanov, Effect of pressure on raman spectra of SnS$_2$ single crystals, Phys. Solid State 52 (2010) 352.

[12] B. Palosz, W. Steurer, H. Schulz, Refinement of SnS$_2$ Polytypes 2H, 4H and 18R, Acta Crystallogr. Sect B 46 (1990) 449.

[13] A. Yella, E. Mugnaioli, H.A. Therese, M. Panthofer, U. Kolb, W. Tremel, Synthesis of fullerene- and nanotube-Like SnS$_2$ nanoparticles and Sn/S/Carbon nanocomposites, Chem. Mater. 21 (2009) 2474.

[14] S.Y. Hong, R. Popovitz-Biro, Y. Prior, R. Tenne, Synthesis of SnS$_2$/SnS fullerene-like nanoparticles: A superlattice with polyhedral shape, J. Am. Chem. Soc. 125 (2003) 10470.

[15] G. Radovsky, R. Popovitz-Biro, M. Staiger, K. Gartsman, C. Thomsen, T. Lorenz, et al., Synthesis of copious amounts of SnS$_2$ and SnS$_2$/SnS nanotubes with ordered superstructures, Angew. Chem. Int. Ed. 50 (2011) 12316.

[16] Y. Sun, H. Cheng, S. Gao, Z. Sun, Q. Liu, Q. Liu, et al., Freestanding tin disulfide single-layers realizing efficient visible-light water splitting, Angew. Chem. Int. Ed. 51 (2012) 8727.

[17] G. Domingo, R.S. Itoga, C.R. Kannewurf, Fundamental optical absorption in SnS$_2$ and SnSe$_2$, Phys. Rev. 143 (1966) 536.

[18] C. Xia, J. An, T. Wang, S. Wei, Y. Jia, Sn$_{1-x}$Ti$_x$S$_2$ ternary alloys: A new visible optical material, Acta Mater. 72 (2014) 223.

[19] A. Sanchez-Juarez, A. Ortiz, Effects of precursor concentration on the optical and electrical properties of Sn$_x$Sy thin films prepared by plasma-enhanced chemical vapour deposition, Semicond. Sci. Technol. 17 (2002) 931.

[20] H.S. Im, Y. Myung, Y.J. Cho, C.H. Kim, H.S. Kim, S.H. Back, et al., Facile phase and composition tuned synthesis of tin chalcogenide nanocrystals, RSC Adv. 3 (2013) 10349.

[21] H. Geng, Y. Su, H. Wei, M. Xu, L. Wei, Z. Yang, et al., Controllable synthesis and photoelectric property of hexagonal SnS_2 nanoflakes by Triton X-100 assisted hydrothermal method, Mater. Lett. 111 (2013) 204.

[22] P. Cai, D.K. Ma, Q.C. Liu, S.M. Zhou, W. Chen, S.M. Huang, Conversion of ternary Zn_2SnO_4 octahedrons into binary mesoporous SnO_2 and hollow SnS_2 hierarchical octahedrons by template-mediated selective complex extraction, J. Mater. Chem. A 1 (2013) 5217.

[23] R. Wei, J. Hu, T. Zhou, X. Zhou, J. Liu, J. Li, Ultrathin SnS_2 nanosheets with exposed {001} facets and enhanced photocatalytic properties, Acta Mater. 66 (2014) 163.

[24] J. Li, Z. Yang, Y. Tang, Y. Zhang, X. Hu, Carbon nanotubes-nanoflake-like SnS_2 nanocomposite for direct electrochemistry of glucose oxidase and glucose sensing, Biosens. Bioelectron. 41 (2013) 698.

[25] J. Morales, C. Perez-Vicente, J.L. Tirado, Chemical and electrochemical lithium intercalation and staging in 2H SnS_2, Solid State Ionics 51 (1992) 133.

[26] D.G. Clerc, D.A. Cleary, Lithium intercalation into cobaltocene-intercalated tin disulfide ($SnS_2\{CoCp_2\}_x$), Chem. Mater. 6 (1994) 13.

[27] C. Julien, C. Perez-Vicente, Vibrational studies of lithium-intercalated SnS_2, Solid State Ionics 89 (1996) 337.

[28] T. Brousse, S.M. Lee, L. Pasquereau, D. Defives, D.M. Schleich, Composite negative electrodes for lithium ion cells, Solid State Ionics 113–115 (1998) 51.

[29] J.W. Seo, J.T. Jang, S.W. Park, C. Kim, B. Park, J. Cheon, Two-dimensional SnS_2 nanoplates with extraordinary high discharge capacity for lithium ion batteries, Adv. Mater. 20 (2008) 4269.

[30] J. Ma, D. Lei, L. Mei, X. Duan, Q. Li, T. Wang, et al., Plate-like SnS_2 nanostructures: Hydrothermal preparation, growth mechanism and excellent electrochemical properties, CrystEngComm 14 (2012) 832.

[31] J. Ma, D. Lei, X. Duan, Q. Li, T. Wang, A. Cao, et al., Designable fabrication of flower-like SnS_2 aggregates with excellent performance in lithium-ion batteries, RSC Adv. 2 (2012) 3615.

[32] D. Lei, M. Zhang, B. Qu, J. Ma, Q. Li, L. Chen, et al., Hierarchical tin-based microspheres: Solvothermal synthesis, chemical conversion, mechanism and application in lithium ion batteries, Electrochim. Acta 106 (2013) 386.

[33] Q. Wu, L. Jiao, J. Du, J. Yang, L. Guo, Y. Liu, et al., One-pot synthesis of three-dimensional SnS_2 hierarchitectures as anode material for lithium-ion batteries, J. Power Sources 239 (2013) 89.

[34] B. Qu, C. Ma, G. Ji, C. Xu, J. Xu, Y.S. Meng, et al., Layered SnS_2-reduced graphene oxide composite – A high-capacity, high-rate, and long-cycle life sodium-ion battery anode material, Adv. Mater. 26 (2014) 3854.

[35] X. Xie, D. Su, S. Chen, J. Zhang, S. Dou, G. Wang, SnS_2 nanoplatelet@graphene nanocomposites as high-capacity anode materials for sodium-ion batteries, Chem. Asian J. 9 (2014) 1611.

[36] T.J. Kim, C. Kim, D. Son, M. Choi, B. Park, Novel SnS_2-nanosheet anodes for lithium-ion batteries, J. Power Sources 167 (2007) 529.

[37] S. Liu, X. Yin, L. Chen, Q. Li, T. Wang, Synthesis of self-assembled 3D flowerlike SnS_2 nanostructures with enhanced lithium ion storage property, Solid State Sci. 12 (2010) 712.

[38] Y. Zou, Y. Wang, Microwave solvothermal synthesis of flower-like SnS_2 and SnO_2 nanostructures as high-rate anodes for lithium ion batteries, Chem. Eng. J. 229 (2013) 183.

[39] X.L. Gou, J. Chen, P.W. Shen, Synthesis, characterization and application of SnS_x (x = 1, 2) nanoparticles, Mater. Chem. Phys. 93 (2005) 557.

[40] F. Tan, S. Qu, W. Ju, K. Liu, S. Zhou, Z. Wang, Preparation of SnS_2 colloidal quantum dots and their application in organic/inorganic hybrid solar cells, Nanoscale Res. Lett. 6 (2011) 298.

[41] T. Havlik, P. Balaz, Z. Bastl, J. Briancin, R. Kammel, Composition and surface analysis of mechanochemically synthetized tin sulfide, Kovove Mater. 34 (1996) 376.

[42] P. Balaz, Z. Bastl, T. Havlik, J. Lipka, I. Toth, Characterization of mechanosynthetized sulphides, Mater. Sci. Forum 235–238 (1997) 217.

[43] P. Balaz, T. Ohtani, Mechanosynthesis of a new tin sulphide phase, Mater. Sci. Forum 343–346 (2000) 389.

[44] P. Balaz, L. Takacs, T. Ohtani, D.E. Mack, E. Boldizarova, V. Soika, et al., Properties of a new nanosized tin sulphide phase obtained by mechanochemical route, J. Alloys Compd. 337 (2002) 76.

[45] B.H. Toby, EXPGUI, a graphical user interface for GSAS, J. Appl. Cryst. 34 (2001) 210.

[46] A.C. Larson, R.B. Von-Dreele. General structure analysis system (GSAS). Los Alamos Natl. Lab. Rep.-LAUR (1994) 86–748.

[47] D. Stroud, Generalized effective-medium approach to the conductivity of an inhomogeneous material, Phys. Rev. B 12 (1975) 3368.

[48] S.J. Clark, M.D. Segall, C.J. Pickard, P.J. Hasnip, M.J. Probert, K. Refson, et al., First principles methods using CASTEP, Z. Kristallogr. 220 (2005) 567.

[49] V.G. Hadjiev, D. De, H.B. Peng, J. Manongdo, A.M. Guloy, Phonon probe of local strains in SnS_xSe_{2-x} mixed crystals, Phys. Rev. B 87 (2013) 104302.

[50] A. Brudnik, A. Gorzkowska-Sobas, E. Pamula, M. Radecka, K. Zakrzewska, Thin film TiO_2 photoanodes for water photolysis prepared by dc magnetron sputtering, J. Power Sources 173 (2007) 774.

[51] C. Suryanarayana, Mechanical alloying and milling, Prog. Mater. Sci. 46 (2001) 1.

[52] M.I. Katanelaon, Graphene: Carbon in two dimensions, Mater. Today 10 (2007) 20.

[53] F.A.S. Al-alamy, A.A.B. Balchin, M. White, The expansivities and the thermal degradation of some layer compounds, J. Mater. Sci. 12 (1977) 2037.

[54] F. Delogu, Ag-Ni Janus nanoparticles by mechanochemical decomposition of Ag and Ni oxalates, Acta Mater. 66 (2014) 388.

[55] T. Matsutani, K. Yamasaki, H. Tsutsui, T. Miura, T. Kawasaki, Amorphous SiCN diaphragm for transmission electron microscope with environmental-cell fabricated by plasma-enhanced chemical vapor deposition, Vacuum 88 (2013) 83.

[56] M. Cruz, J. Morales, J.P. Espinos, J. Sanz, XRD, XPS and ^{119}Sn NMR study of tin sulfides obtained by using chemical vapor transport methods, J. Solid State Chem. 175 (2003) 359.

[57] M. He, L.X. Yuan, Y.H. Huang, Acetylene black incorporated three-dimensional porous SnS_2 nanoflowers with high performance for lithium storage, RSC Adv. 3 (2013) 3374.

[58] L. Jie, X. Chao, XPS examination of tin oxide on float glass surface, J. Non-Cryst. Solids 119 (1990) 37.

[59] J. Yin, H. Cao, Z. Zhou, J. Zhang, M. Qu, SnS_2@reduced graphene oxide nanocomposites as anode materials with high capacity for rechargeable lithium ion batteries, J. Mater. Chem. 22 (2012) 23963.

[60] T. Shimada, F.S. Ohuchi, B.A. Parkinson, Thermal decomposition of SnS_2 and $SnSe_2$: Novel molecularbeam epitaxy sources for sulfur and selenium, J. Vac. Sci. Technol., A 10 (1992) 539.

[61] P. Kubelka, F. Munk, A contribution to the optics of pigments, Z. Technol. Phys. 12 (1931) 593.

[62] E. Rosencher, B. Vinter, Optoelectronics, Cambridge University Press, Cambridge, 2004.

[63] C. Julien, M. Eddrief, I. Samaras, M. Balkanski, Optical and electrical characterizations of SnSe, SnS_2 and $SnSe_2$ single crystals, Mater. Sci. Eng., B 15 (1992) 70.

[64] H.L. Zhang, R.G. Hennig, Theoretical perspective of photocatalytic properties of single-layer SnS_2, Phys. Rev. B 88 (2013) 115314.

[65] M. Radecka, M. Rekas, A. Trenczek-Zajac, K. Zakrzewska, Importance of the band gap energy and flat band potential for application of modified TiO_2 photoanodes in water photolysis, J. Power Sources 181 (2008) 46.

[66] H. Guo, H. Zhao, X. Jia, X. Li, W. Qiu, A novel microspherical $CoSn_2$/Sn alloy composite as high capacity anode materials for Li-ion rechargeable batteries, Electrochim. Acta 52 (2007) 4853.

[67] S. Liu, X. Lu, J. Xie, G. Cao, T. Zhu, X. Zhao, Preferential c-axis orientation of ultrathin SnS_2 nanoplates on graphene as high-performance anode for Li-ion batteries, ACS Appl. Mater. Interfaces 5 (2013) 1588.

[68] K. Hiral, T. Ichitsubo, T. Uda, A. Miyazaki, S. Yagi, E. Matsubara, Effects of volume strain due to Li–Sn compound formation on electrode potential in lithium-ion batteries, Acta Mater. 56 (2008) 1539.

[69] Y. Ein-Eli, V.R. Koch, Chemical oxidation: A route to enhanced capacity in Li-ion graphite anodes, J. Electrochem. Soc. 144 (1997) 2968.